

A novel portable, high-luminosity monochromatically tuneable X-ray microscope.

F. Flora¹, S. Bollanti¹, A. Lai¹, P. Di Lazzaro¹, T. Letardi¹, A. Grilli², L. Palladino³, G. Tomassetti³, A. Reale³, L. Reale³, A. Scafati³, L. Bacchetta⁴, L. Alianelli⁵, M. Sanchez del Rio⁶, T.A. Pikuz⁷, A. Ya. Faenov⁷

¹ENEA, Dipartimento Innovazione, Settore Fisica Applicata, 00044 Frascati, Italy

²INFN Frascati, 00044 Frascati, Italy

³INFN Dipartimento di Fisica dell'Aquila and LNGS-INFN, Assergi (L'Aquila), Italy

⁴Agriculture biotechnology Department, ENEA C.R. Casaccia, Via Anguillarese 301, 00060, Roma

⁵INFN-OGG c/o ESRF, BP 220, F-38043 Grenoble Cedex, France, and ILL, BP 156, F-38042 Grenoble Cedex

⁶European Synchrotron Radiation Facility, BP 220, F-38043 Grenoble Cedex, France

⁷Multicharged Ions Spectra Data Center of VNIIFTRI, Mendeleevo, Moscow region, 141570 Russia

Abstract.

A novel experimental setup for transmission x-ray microscopy is presented. It is based on the use of a point isotropic x-ray source and a single spherical crystal. The x-ray beam intensity is modulated by the object attenuation, then monochromatized and enlarged using a spherical crystal and, lastly, imaged using a detector downstream of the crystal. We demonstrate by ray tracing technique and experimental testing that this system allows microscopy studies with image resolution better than the dimensions of the source, high magnification ratios, and great field of view. Microscopes using this model can be easily built using different micro x-ray sources, like conventional x-ray tube generators, x-rays emitted by laser generated plasmas or synchrotron radiation. Utilization of spherically bent crystals to obtain high-resolution, large field, monochromatic images in a wide range of Bragg angles ($20^\circ < \Theta < 45^\circ$) is demonstrated for the first time. High quality monochromatic ($\delta\lambda/\lambda \sim 10^{-5} - 10^{-3}$) images with high magnification about 15-35 times and spatial resolution ($< 10 \mu\text{m}$) over a large field of view (few mm^2) were obtained. Some possible applications and preliminary experimental verification of the feasibility of the setup are also presented.

Keywords: X-ray optics, X-ray backlighting, laser plasma diagnostics

Introduction.

X-ray optics presented an unprecedented development in the recent years allowing sub-micron x-ray microprobes. Reflecting (Kirkpatrick-Baez configuration of mirrors or multilayers), refracting (Compound Refracting Lenses) and diffracting (Fresnel zone plates, Bragg-Fresnel and perfect crystals) systems are presently in use. Reviews on instrumentation for x-ray microscopy with photon energy below and above 1 keV are available (see, for example, Ref. ¹⁻⁴). Synchrotron sources are the preferred x-ray sources in terms of brightness, and presently almost every facility has one or several types of x-ray microscopy beamlines. However, they require large installation and in many cases present difficult access. X-ray tubes have the advantage of being accessible in many small laboratories. A variation of the x-ray tube useful for microscopy applications can be obtained from a simple modification of an electron microscope². Another way to create x-rays is the use of a laser-produced plasma, generated by the interaction of intense pulsed (femtosecond, picosecond or nanosecond) lasers with a solid target, or an x-pinch plasma. In such cases, the pulsed x-rays are emitted isotropically from the interaction zone of dimension of 5-100 μm . Recent developments in laser technology allow compact powerful lasers designed to produce table-top x-ray sources for customized applications.

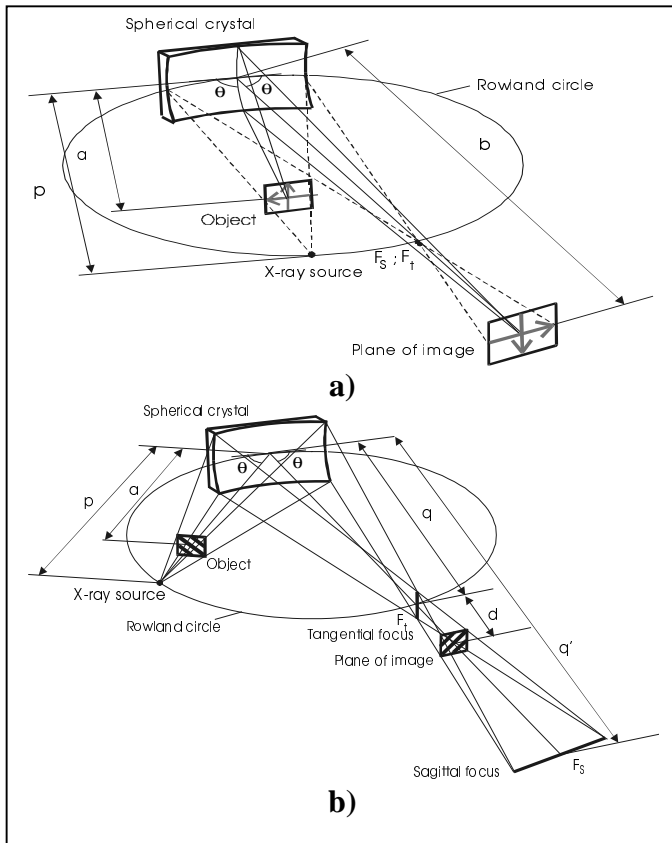
Two main approaches are used for x-ray microscopy: to scan the object (sample) illuminated by an x-ray microprobe, for obtaining images of the transmitted photons or fluorescence or secondary electrons (scanning microscopy); and to magnify the x-ray image itself by an optical system (imaging microscopy). The simplest way to create an imaging microscope is to record the projected image of the object when illuminated by a point isotropic source (projection microscopy)⁵. Here, the object is placed between the source and the detector (e.g., an x-ray film). The magnification is given by the ratio of source-film to source-object distance. The transversal spatial resolution is limited by the size of the source and diffraction effects. Such techniques is successfully applied now when x-ray tubes with well-focused electron beams (0.1 μm)

were available⁶. Another type of imaging microscope is the “Göttingen” transmission microscope⁷, which uses two zone plates.

In this paper an *X-ray Crystal Imaging Microscope* (XCIM) is considered. On one hand, it can be seen as a variation of the projection microscope, consisting in inserting a spherically crystal between the object and the film. Among the advantages of the XCIM respect to the projection microscope, which is basically a microscope without optics, we can mention: i) the monochromatization of the radiation by the crystal, improving the quality of the image, ii) the flexibility of designing an instrument considering the fact that there are more parameters than simply the distances ratio, and iii) the resolution depends on the source dimension, but is not limited by it (resolution better than source dimension can be obtained). On the other hand, it can be considered as an improvement of imaging crystal spectrometers or backlighting schemes with spherically bent crystals⁸⁻¹⁰ in use for plasma diagnostics and applications. The surface of dense laser-produced plasmas is hot enough to produce significant quantities of x-rays to be used to characterize the plasma of for illuminating other objects to be imaged. Large magnified x-ray images have been obtained using spherically curved crystals in normal incidence¹¹⁻¹³ or toroidally¹⁴ curved crystals to relax the backscattering condition. The XCIM has many advantages compared with existing configurations. The spherical crystal is simpler to manufacture, easier to align and can be used in a multitude of distance configurations and Bragg angles as compared to a toroidal crystal. The XCIM produces high resolution quasi-undistorted images for any Bragg angle, thus allowing a higher spectral tunability and higher field of view than conventional backscattering schemes. The considered microscope uses a point-like isotrope source, thus it is in principle targeted for applications using x-ray sources like x-ray tubes or point plasma x-ray sources. However, it can also be used for synchrotron radiation applications when combined with other condensing optics.

II. Description of the microscope setup

The microscope system can be considered as a modification of the x-ray backlighting system⁸⁻¹³, which is demonstrated a successful tool in imaging laser-generated plasmas. In the traditional x-ray backlighting scheme (see Fig. 1a) a spherically curved crystal (with curvature radius R) is placed on the Rowland circle of radius $R/2$.



The x-ray source (backlighter) is on the Rowland circle and is imaged on another point of the Rowland circle. Placing a detector (i.e., an x-ray film or CCD camera) downstream from the focal image of the source, it is possible to obtain an enlarged image of the source, with different magnification depending on the distance from focal-point to detector. If the backlighter dimensions are small (quasi-point source) and an object is placed at a distance a upstream from the crystal, then a transmission image (radiography) of the object will be observed in the detector plane at a distance b downstream from the crystal. The distances a and b are related by the lens equation $1/a+1/b = 2/(R \sin\theta)$. The magnification of this system is $M=(b-p)/(p-a)$ (in both the tangential and sagittal planes). The magnification can be increased by either approaching the object to the source (i.e., $p-a$ tends to zero) or by moving away the detector (increasing b). It is important to note that the object can be positioned at any place between the source and the crystal, and, more important, the position of the detector is also free. This imaging transmission microscope only works for a limited interval of Bragg angles¹⁰ (80-90 deg), otherwise the aberrations (astigmatism) strongly deteriorate the image. In addition, the spectral tunability of the system is reduced because it is only possible to work at wavelengths close to multipliers of $2d$ (the d -spacing of the crystal lattice). One of the most important features of the proposed XCIM system (Fig. 1 b) is the relaxation of the normal incidence condition. It can also work out of the Rowland configuration. Moreover, the detector cannot be placed at any place downstream from the focal point, as for the traditional backlighting scheme, but must be positioned

at a fixed distance d from the tangential focus (see below). When considering a curved mirror or crystal with a radius of curvature R set to receive x-rays from the source (placed at distance p from the center of the crystal) with a grazing (Bragg) angle θ , two focal images at distances q and q' are formed. They correspond to the tangential and sagittal foci, respectively. The focal position for the tangential plane q is obtained from:

$$1/p + 1/q = 2/[R \sin \theta] \quad (1)$$

and the focal distance q' for the sagittal plane is given by:

$$1/p + 1/q' = 2 \sin \theta / R \quad (2)$$

The formulas (1) and (2) are the extension for grazing incidence of ordinary geometric optics principles for mirrors¹⁵. In the particular case of normal incidence ($\theta=90$ deg) both foci are coincident ($q=q'$). Another important particular case that satisfies eq. (1) is when the source, the crystal and the tangential focal point lie on a circle of radius $R/2$, the so-called Rowland circle. The Rowland circle configuration optimizes, at the same time, the energy bandwidth of the diffracted beam and the focalization. In our case, using symmetric Bragg crystals, this condition is satisfied if $p=q=R \sin \theta$.

Let us now analyze the behavior of this system as an x-ray microscope: consider a small object in the path of the rays at a distance a upstream from the pole of the crystal and calculate the position where the “best” image is found. We can define the “best” image as the one with presents the same magnification in both the sagittal and tangential plane. Therefore, the image is as “undistorted” as possible and presents the same aspect ratio as the imaged object. It can be easily shown that this image is found when the detector is positioned at a distance d downstream from the tangential focus:

$$d = (q'q - q^2)/(q' + q) \quad (3)$$

Let us denote with Ω_i the incident divergence. Ω_r and Ω_r^{sag} are the reflected divergences in the tangential and sagittal planes, respectively. The focusing condition guarantees that $p \Omega_i = q \Omega_r = q' \Omega_r^{\text{sag}}$. The magnification in the tangential plane at the “best image” position can be calculated as

$$M = \frac{\Omega_r}{\Omega_i} \frac{d}{(p-a)} = \frac{p}{q} \frac{d}{(p-a)} \quad (4)$$

With the help of equation (1) we obtain

$$M = \frac{d [2p - R \sin \theta]}{R p \sin \theta (1 - a/p)} \quad (5)$$

If we let a/p be a varying parameter, and using equations (1), (2) and (3), we can express M as a function of only p , R , and the Bragg angle:

$$M = \frac{p[1 - \sin^2 \theta]}{p[1 + \sin^2 \theta] - R \sin \theta} \cdot \frac{1}{1 - a/p} \quad (6)$$

The magnification in the tangential plane is:

$$M_s = \frac{\Omega_r^{\text{sag}}}{\Omega_i} \frac{q' - (q+d)}{p-a} = \frac{(1 - (q+d)/q')}{(1 - a/p)} \quad (7)$$

Eqs. (4) and (7) are the general expression for the magnification in the tangential and sagittal directions, respectively. The position of the detector (i.e., best image given by Eq. (3)) does not depend on the position of the object a . However, contrarily to what happens in the traditional backlighting scheme, where the detector can be positioned anywhere, the detector position depends now on the focal distances q and q' . Therefore, images with different magnifications can be obtained by simply moving the object (i.e., changing a in Eq. (6)) whilst keeping fixed the crystal and detector.

Particular case: the source is located on the Rowland circle

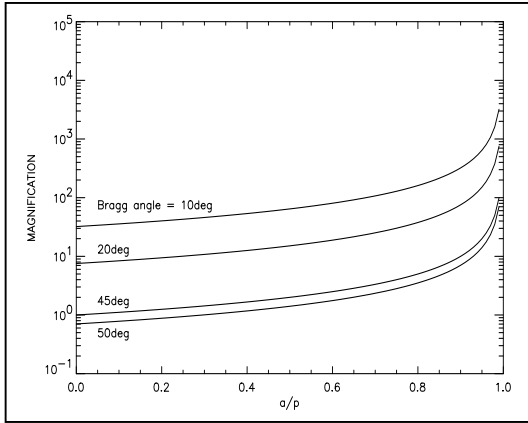
In the particular case that the source, crystal and tangential focus are placed on the Rowland circle we have

$$p = q = R \sin \theta \quad (8)$$

therefore, the magnifications takes the form:

$$M = \cotg^2 \theta \cdot \frac{1}{1 - a/p} \quad (9)$$

M as a function of a/p only depends on the Bragg angle. For a given Bragg angle, M ranges from $\cotg^2 \theta$ to infinity depending on the relative distance source-object. On the other hand, if we fix a/p , then M can be made as large as wanted by decreasing the Bragg angle. This equation shows some fundamental aspects of the proposed setup: i) one can obtain, in principle, a magnification as high as wanted, ii) for increasing magnification one can choose between going to more grazing Bragg angles or approaching the object to the source (or a combination of both), and iii) Bragg angles more (less) grazing



Bragg angles or approaching a to p), some experimental limitations arise: for a given crystal size, the accepted divergence Ω_i is smaller when M is increased; and the field of view (or object dimension) must be smaller for a given divergence Ω_i when one approaches a to p . Fig 2 shows a plot of M versus a/p for several Bragg angles. From Fig. 2, and considering previous experimental works¹⁵, we have selected the parameters of a initial configuration that will be the “*basic configuration*” for our ray tracing studies. We selected $R=15$ cm and a Bragg angle of 20 deg. Source and crystal are mounted in a Rowland circle configuration with $p=q=5.13$ cm and $q+d=43.86$ cm. When $a=3.5$ cm, the magnification is about 24. The crystal size is about $15 \times 50 \text{ mm}^2$. The x-ray source considered here emits isotropic radiation. We will study the effect of the source dimensions ranging from zero (point source) to several tens of microns (a typical laser generated plasma has source size of not less than $20 \mu\text{m}$).

III. Image production modeling.

3.1. Ray tracing calculations

The performance of a system consisting of an x-ray source and a curved crystal is analyzed by L. Alainelli and M. Sanchez del Rio using ray-tracing simulations. The x-ray source was represented by either a point source or a 3-dimensional cylindrical source. In the latter case, the rays are created inside a cylinder (of several diameter and length values) which axis is directed along the optical axis (the line between the source center and the crystal center). It is assumed that the source emits isotropically in all directions. In the simulations, for efficiency reasons, the rays are emitted into a reduced solid angle (defined by the semi-aperture of the emission cone, usually between 0.1 and 0.01 rad) which illuminates a limited area of the crystal up to the dimensions corresponding to the physical size of the available crystals (about $15 \times 50 \text{ mm}^2$). The crystal is placed at a distance p from the source, and is orientated to the required Bragg angle relative to the incoming beam. The crystal is considered as a “mirror-like” system, which means that each ray is reflected at the crystal surface following the laws of specular reflection (incident ray, surface’s normal and reflected ray must lie on the same plane; and reflected angle equals the incident angle). The validity of this approximation has been discussed elsewhere¹⁶. In a real crystal, the diffraction process takes place in a crystal volume determined by the primary extinction depth. Although this length is small for perfect crystals, it may degrade the spatial resolution of an imaging system like the one considered here. This effect limits the resolution of the microscope and is also studied by ray tracing. For that reason, mosaic crystals where the penetration of the beam inside the crystal is much larger (defined by the secondary extinction length) are less suitable for this type of microscope. Therefore, the perfection of the crystal is an important parameter to consider when designing a crystal microscope because it determines the best available resolution.

Ray-tracing calculations were performed using the SHADOW package¹⁷. Typical runs use 5000 rays. Several simulations have been performed to study the role of the different system parameters in the quality of the image. The goal was to obtain high magnification rates ($M>10$) with spatial resolution of the order of microns, when using x-ray sources with dimension of several microns and spherically bent crystals with radii in the interval 8-20 cm. We show how the quality of the image (uniformity of magnification and spatial resolution) is influenced by experimental parameters like geometrical errors of the crystal figures (uniformity of the curvature radius), crystal size or entrance pupil, source depth and size, and grazing Bragg angle. The results of this study can then be used to design a suitable XCIM to match the user requirements.

3.2 Ray tracing results

3.2.1. Results for the basic configuration

Several ray-tracing experiments have been performed to confirm the validity of the formulas (3) to (9). A source that emits “rays” randomly distributed in a cone of semi-aperture either 0.01 or 0.1 rad has been used. It emits isotropic radiation and have dimensions of either zero (point source) or $20 \mu\text{m}$. The crystal parameters are: $R=15$ cm and $\theta=20$ deg. The source and crystal are located on the Rowland circle with $p=q=5.13$ cm. The best image position is found at $q+d=43.86$ cm ($d=38.72$ cm). When $a=3.5$ cm, the magnification is $M=23.76$.

In Fig. 3 we can see the calculated image produced by an absorbing mesh grid of $120 \mu\text{m}$ period and $14 \mu\text{m}$ thickness imaged at the object position and at the detector position. Two images are presented: the mesh grid (object) plane

and the detector (image) plane. A first run has been done using a beam divergence of 0.01 rad. A 20 μm diameter source with height of 1mm has been used. The image at the detector plane (Fig 3b) shows some important facts: i) the 14 μm thick

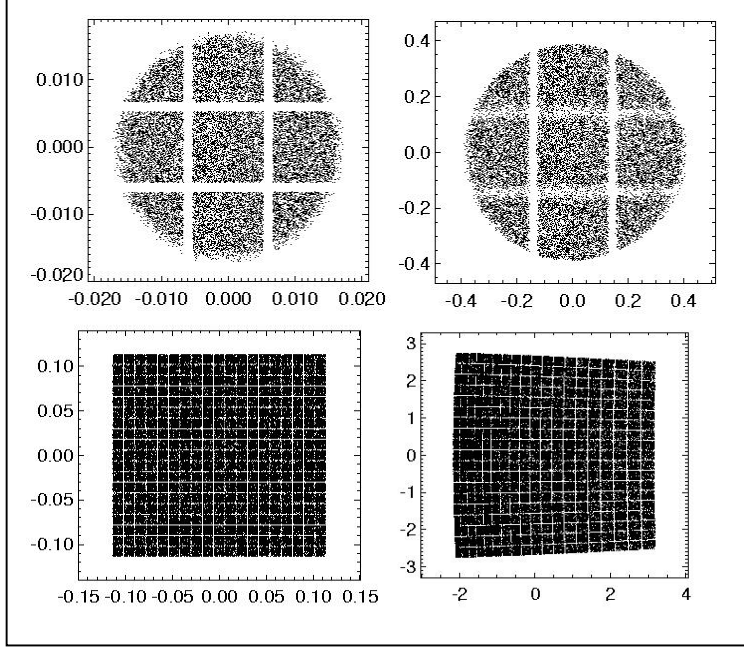


Fig 3. Ray tracing results for the basic configuration: $R=15$ cm; source located on the Rowland circle: $p=q=5.13$ cm; $q+d=43.86$ cm ; $a=3.5$ cm, and $M\approx 24$. The grid period and thickness are 120 and 14 μm , respectively. The image on the left represents the grid (object plane). The image on the right shows the image of the grid in the image plane. Note that the scales of the two graphs are different, showing a magnification about $M=24$. Top) The source is a cylinder of diameter equal to 20 μm and height equal to 1mm which emits randomly in a cone of semiaperture 0.01 rad. Bottom) The source has no dimensions (point source) and its divergence (semiaperture) is 0.1 rad.

wires are perfectly visible (demonstrating high spatial resolution, better than the source size), ii) the image presents the same aspect ratio in tangential (diffraction) and sagittal planes, and iii) the spatial resolution is better in the tangential plane (horizontal direction in the figure) than in the sagittal one (vertical in the figure). We want to emphasize that these results are obtained for a Bragg angle ($\theta=20\text{deg}$) far from backscattering, and are confirmed by experimental tests (see below).

In the traditional backlighting scheme, for a given crystal setup (i.e., fixing p , R and θ) there is an infinity of pairs of values (a,b) that gives the same magnification M . In the case of non-normal incidence, there is, however, only one pair that produces an image with the same aspect ratio as the object, and this is the one that corresponds to the XCIM case. In other words, the XCIM setup is the same as the traditional backlighting scheme, but the degeneration in the solution for (a,b) is broken to fulfill the condition of identical aspect ratio for the image and object. A second SHADOW run has been done using a point source of divergence 0.1 rad. In this case, the size of the illuminated object (field of view) is 3 mm, and the footprint on the crystal (tangential direction) is 15 mm. The result (Fig. 3d) still shows a high resolution image, but with an appreciable distortion in regions far from the center.

3.2.2. Change in magnification due to object thickness or object displacement

In a real experiment, the object to be imaged is not a plane but a volume, thus it has a given thickness in the beam direction. In consequence, if we consider the object to be composed by a collection of thin slices in the beam direction, each slice will be positioned in a different object plane (i.e., different a value) and then each slice will be affected by a different magnification M . This implies an aberrated image due to the fact that parts of the object closer to the source are more magnified than the parts farther from the source. An equivalent effect is obtained when displacing a plane object in direction parallel to the beam.

Let us study how M changes with respect to its mean value as a function of a small change of the parameter a . Calling Δa the thickness and/or the error on the object position, we can calculate its effect on magnification and then check it with ray-tracing. When θ and p are kept fixed, the change in magnification due to Δa is

$$\Delta M = \left(\frac{\partial M}{\partial a} \right)_{p,\theta} \Delta a \quad (10)$$

therefore

$$\left(\frac{\Delta M}{M} \right)_{p,\theta} = \Delta a / (p - a) \quad (11)$$

If we think in different experimental configurations defined by pairs (R, θ) which give the same M , then the most critical configurations are those for which $(p-a)$ is small. For a given R , $(\Delta M/M)_{p,\theta}$ is larger at high Bragg angles because in this case one has to put $a/p \rightarrow 1$ in order to obtain the wanted magnification M . $(\Delta M/M)_{p,\theta}$ also increases when decreasing R if both θ and a/p are fixed. Table 1 shows the results of both ray-tracing and analytical calculations for three pairs (R, θ) which give

approximately the same magnification ($M \sim 24$). A value of $\Delta a = 1$ mm has been considered. When both θ and a/p are fixed, then $(\Delta M/M)_{p,\theta} \propto \Delta a/R$; when, instead, we increase θ , we have to make a/p closer to 1 in order to get the relative change in

Table 1 Change in magnification due to object thickness or position error Δa . The magnification values are calculated exactly, and relative variations of M calculated by Eq. (11) are compared with values obtained by ray-tracing.

Theta (deg)	Radius (cm)	p (cm)	a (cm)	Δa (cm)	Magnification		Relative variation of M			
					sagittal	tangential	ray-tracing		calculated	
							sagittal	tangential	sagittal	tangential
20	15	5.13	3.5	0	23.7	23.7				
			3.4	-0.1	22.4	22.2	-5.4%	-6.3%	-6.0%	
			3.6	0.1	25.3	25.4	6.6%	6.9%	6.3%	
20	25	8.55	5.85	0	24.0	24.0				
			5.75	-0.1	23.3	23.1	-3.0%	-3.6%	-3.6%	
			5.95	0.1	24.9	24.7	3.6%	3.0%	3.8%	
45	25	17.68	16.94	0	24.0	24.0				
			16.84	-0.1	20.4	20.6	-14.9%	-14.3%	-12.7%	
			17.04	0.1	27.9	27.9	16.1%	16.1%	14.5%	

magnification increases. From these results we can conclude that the XCIM is not very sensitive to the object thickness or displacements, thus making it suitable for imaging three-dimensional objects

3.2.3. Change in magnification due to uncertainty on the radius of curvature or Bragg angle

When R and/or θ change the variations of M have to be calculated after considering the following: i) we are no longer in the Rowland circle, so the general expression for M has to be considered; ii) such a expression is not the same for the tangential and sagittal directions; iii) the image we look at is no more the best image; our image is located at a distance d from the tangential focus that is given by $d = d_0 + \Delta d$ with d_0 the distance for the unperturbed system given by Eq. (3), and $\Delta d = -\Delta q = q_0 - q$, the difference between the distances to the tangential focus for the unperturbed and perturbed systems; and iv) the factor $1/(1 - a/p)$ remains unchanged. Eq. (4) and (7) give the magnification in the tangential and sagittal directions, respectively. When R and/or θ change we have

$$(\Delta M / M)_{a,p}^{sag} = \Delta q' / q' \times [(d_0 + q_0) / (q'_0 - q_0 - d_0)] \quad (12)$$

$$(\Delta M / M)_{a,p}^{tan} = -\Delta q / q \times [(d_0 + q_0) / (d_0 - \Delta q)] \quad (13)$$

for the sagittal and tangential planes, respectively. For the basic system, $q_0, q'_0 \ll d_0$, then:

$$(\Delta M / M)_{a,p}^{sag} = -(\Delta q' / q')_{a,p} \quad (14)$$

$$(\Delta M / M)_{a,p}^{tan} = -(\Delta q / q)_{a,p} \quad (15)$$

From Eqs. (14) and (15) one obtains the change in M in the sagittal and tangential planes, respectively, related to the change in R :

$$(\Delta M / M)_{a,p,\theta}^{sag} = (\Delta R / R) [1 - R / (2p_0 \sin \theta)] \quad (16)$$

$$(\Delta M / M)_{a,p,\theta}^{tan} = -(\Delta R / R) [1 - R / (2p_0 \sin \theta)] \quad (17)$$

In a similar way, the change of magnification respect to variations in Bragg angle is:

$$(\Delta M / M)_{a,p,R}^{sag} = \frac{\cot \theta}{1 - R / (2p_0 \sin \theta)} \Delta \theta \quad (18)$$

$$(\Delta M / M)_{a,p,R}^{tan} = -\frac{\cot \theta}{1 - (R / 2p_0) \sin \theta} \Delta \theta \quad (19)$$

Comparisons between calculated values using these formulas with ray tracing results are shown in Table 2. These results verify the stability of the XCIM versus small errors in crystal curvature and Bragg angle

3.2.4. Distortion of the image

We have seen that a distortion of the image appears when the accepted source divergence is large. From Fig. 3a one can see that the image using a 0.01 rad divergent source is mainly undistorted, whereas for a source ten times more divergent (Fig. 3b) the image is slightly distorted, but conserving a good spatial resolution. This means that magnification at the image edges is different than the one at the center of the image. In order to study this effect, we have created a point source with divergence in a grid scale from zero to 0.1 rad. The source projection at the object plane for the basic configuration is in Fig. 4 (left). The magnified image is in Fig. 4 (right). A deformation in the tangential plane (horizontal in the graph) is clearly

seen when the source divergence is increased. Giving a point in the image (a given ray), we can calculate the “local” magnification for that point by calculating the ratio between the distance to the center of the image plane in such an image over the same magnitude in the object plane. That means

$$M_i = \frac{\sqrt{X_i^2 + Y_i^2}}{\sqrt{x_i^2 + y_i^2}} \quad (20)$$

Table 2: Change in magnification due to errors in radius of curvature (table a) and Bragg angle (table b) The magnification values are calculated exactly, and the relative variations of M calculated by Eqs. (14) and (15) in table a and by Eqs. (18) and (19) in table b are compared with values obtained by ray-tracing

Theta (deg)	Radius (cm)	$p_0 = q_0 =$ (cm)	ΔR (cm)	Magnification		ray-tracing		calculated	
				sagittal	tangential	sagittal	tangential	sagittal	tangential
20	15	5.13	0	23.7	23.7				
			0.5	24.0	22.1	1.0%	-6.9%	1.0%	-6.7%
			-0.5	23.6	25.7	-0.6%	8.4%	-1.1%	6.7%

b)

Theta (deg)	Radius (cm)	$p_0 = q_0 =$ (cm)	$\Delta\theta$ (deg)	Magnification		Relative variation of M		ray-tracing		calculated	
				sagittal	tangential	sagittal	tangential	sagittal	tangential	sagittal	tangential
20	15	5.13	0	23.7	23.7						
			0.1	23.7	23.4	0.0%	-1.5%	-0.15%	-0.96%		
			-0.1	23.7	23.9	0.0%	0.9%	0.15%	0.96%		

where (X_i, Y_i) are the coordinates of the i -th ray in the image plane, and (x_i, y_i) are the coordinates in the object plane. The plot of magnification as a function of the polar angle (Fig. 4 right) clearly shows the error in magnification for the different circles corresponding to different source divergences. This error is maximized at the

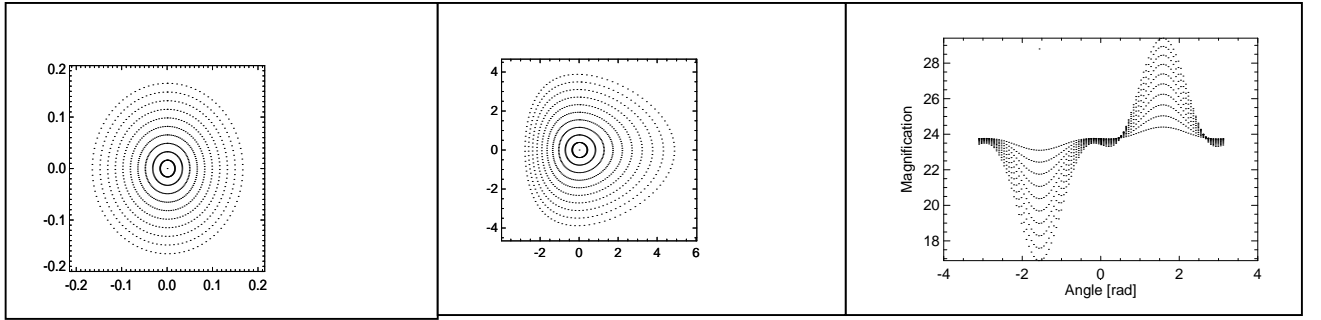


Fig. 4 Grid source imaged in the object plane (left) and in the image plane (center). Units are cm. The magnification for the different points in left figure as a function of the polar angle (right). The origin and direction of the polar angle is shown with a line and an arrow in the top figure.

angles $\pm\pi/2$ (see Fig. 4 right) corresponding to the points more distant from the optical axis in the tangential direction. Clearly, this is distortion effect should disappear if the rays arriving to the crystal surface would satisfy the Abbé sine condition. This law must be verified (at least approximately) by any optical system to form an undistorted image. In grazing incident systems, the magnification for rays coming from a point source that arrive at different positions on the reflecting surface is, in general, different. It can be easily demonstrated that the sine condition cannot be satisfied if only a single reflecting surface is used.

One could think that distortion can be reduced by a small rotation of the detector plane around a vertical axis. Some simulations were done to verify this hypothesis without success: in the best case it is sometimes possible to improve an edge of the image but additional distortions appear in the rest of the image. Other simulations were done using an ellipsoidal crystal. The resulting distortions have similar magnitude than those produced spherical crystals. In conclusion, an ellipsoidal crystal, which eliminates the spherical aberrations in the point-to-point focusing, does not improve the quality of the image because it does not fulfill the sine condition.

3.2.5. Depth of focus

The depth of focus, or more precisely, the allowed detector displacement (errors in d) without significant change in magnification, is very large for the XCIM. Some calculations demonstrate that one can safely move the position of d by several mm without significant distortion of the image. The relation between the magnification and the distance d is linear (Eqs. (14) and (15)). Therefore, a the relative change in magnification due to a displacement Δd of the image is given by:

$$\left(\frac{\Delta M}{M}\right)_{a,p,R,\theta}^{ag} = -\Delta d / (q' - q - d) \quad (21)$$

$$\left(\Delta M / M\right)_{a,p,R,\theta}^{tan} = \Delta d / d \quad (22)$$

The results of the ray tracing compared with those calculated using these formulas are in Table 3. This small sensitivity of the magnification to even large changes in detector position is important for practical applications.

Table 3: Influence of the errors in detector position on the magnification. The magnification values are calculated exactly, and the relative variations of M calculated by Eqs.(21) and(22) are compared with values obtained by ray-tracing

Theta (deg)	Radius (cm)	p= q= (cm)	q' (cm)	Δd (cm)	Magnification		Relative variation of M			
					sagittal	tangential	ray-tracing		calculated	
							sagittal	tangential	sagittal	tangential
20	15	5.13	-6.7	0	23.7	23.7				
				0.5	23.9	24.1	0.9%	1.8%	1.0%	1.3%
				-0.5	23.4	23.4	-1.2%	-1.5%	-1.0%	-1.3%

3.2.6. Spatial resolution versus source dimension

It is essential to have an idea of the achievable resolution when a real source (i.e., an extended source) is used. It is possible to evaluate visually the resulting images of the ray-tracing (e.g., Fig 3) and then assess on the spatial resolution. As an example, from Fig 3 we can say that there is a very good resolution in the tangential plane, a worse resolution in the sagittal one, and in both cases the resolution is better than 14 μm, because the grid wires of this dimension are well resolved. It is convenient to define a method to obtain quantitative value of the spatial resolution from the image scattered plots. For that, histograms of the ray distribution on the “best image” plane are computed in both tangential and sagittal directions. The image of an edge in the object produces some slope in the histogram. From that slope it is possible to determine a value of the spatial resolution. We have fitted the histogram edges to an error function

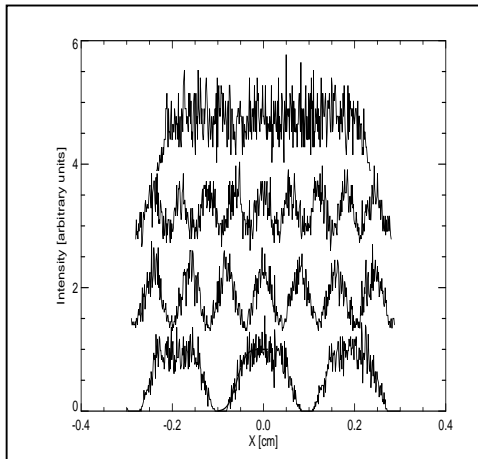


Fig. 5. From bottom to top: 1) resolution histogram at the image plane using a 20 μm source when imaging a grid of $f=30$ μm feature and 80 μm periodicity. The over-plotted thick line is the error function fit of the edge from where the resolution value of $r=17$ μm is obtained. 2) image with the same source produced by a grid with feature $f=r$ and period $2f$. 3) Same as 2) but for $f=0.75 r$. 4) Same as 2) but for $f=0.5 r$.

$$erf(x) = a \int_{-\infty}^x e^{-\left(\frac{x-x_0}{\sigma}\right)^2} dx \quad \text{in order to determine this value. The } \sigma \text{ value}$$

resulting from the fit gives the resolution value $r=2\sigma/M$, with M the magnification. This resolution value means that for a grid of feature f and period $2f$, then if $f=r$ the grid is completely resolved in the image plane (if $f=0.5r$ the grid is not resolved at all; and if $f=0.75r$ the grid is semiresolved). An example to illustrate this fact is reported in Fig. 5. For obtaining good quality histograms (acceptable noise with a small bin step) 50000 rays were used in SHADOW runs. In Table 4 the results of this procedure for different source size are reported. Calculations were done by adjusting the grid feature in order to obtain an histogram with intensity zero in the obscured part. It is possible to clearly resolve features of less than 10 μm in the object using a magnification of $M=24$, and with a source diameter up to about of 20 μm. The source depth can be as large as 1-2 mm.

The results reported in Table 4 show that similar values of resolution as obtained for $R=15$ cm can also be obtained for $R= 8$ and 25 cm ($\theta=20$ deg in both cases). The resolution of the images using a point source is always zero. When the source is not a point, we obtained similar values of the resolution for different R values at $\theta=20$ deg. The resolution is worse at a Bragg angle of 40 deg than of 20 deg when an extended source is used. This effect is due to the fact that when the Bragg angle is increased the object has to be closer to the source in order to obtain the same magnification. Thus, the

3.2.7. Effect of the crystal extinction length in the spatial resolution

In a real crystal, the diffraction effect takes place in a finite volume inside the crystal, and not on the crystal surface. This creates aberrations in the wavefront after diffraction by the crystal. Therefore, a degradation of the in spatial resolution of the XCIM is expected. The beam penetrated into the crystal to a depth that depends on the extinction length, which is given by the dynamical theory of diffraction. When the crystal is perfect, only the primary extinction is responsible for the penetration. Primary extinction length is of the order of few microns (e.g., 32, 28 and 38 microns for mica (004), (006) and (008), respectively, at 8 keV). The penetration depth is increased when the crystal is imperfection increases. For mosaic crystals (ideal imperfect crystals) the effect of the secondary extinction increases the penetration length up to few mm. The penetration effect determines the limiting resolution of the XCIM. In order study it we have modified SHADOW to allow

Table 4. Resolution values for different values of θ , R and source size.

SYSTEM	SOURCE diameter (μm)	Tangential (μm)	Sagittal (μm)
$\theta=20\text{deg}$ $R=8\text{cm}$ $p=2.74\text{cm}$ $a=1.86\text{cm}$	20	4.8	16.2
	40	9.9	32.2
$\theta=20$ $R=15$ $p=5.13\text{cm}$ $a=3.5\text{cm}$	20	4.8	17.0
	40	9.1	33.1
$\theta=20$ $R=25$ $p=8.55\text{cm}$ $a=5.85\text{cm}$	20	5.3	15.9
	40	10.0	34.1
$\theta=20$ $R=100$ $p=34.2\text{cm}$ $a=23.2\text{cm}$	20	5.2	11.8
	40	10.1	32.8
$\theta=40$ $R=25$ $p=16.1\text{cm}$ $a=15.5\text{cm}$	20	12.9	15.8
	40	25.2	31.3

rays to travel inside the crystal a given distance Λ . Let us call Λ_e the mean penetration length, corresponding to the primary extinction length for perfect crystals. It is measured in the direction of the incident ray. A perfect monochromatic collimated beam will penetrate inside the crystal, losing intensity as far as diffracted photons will come in. The probability of a photon to be reflected (i.e., diffracted) after having traveled a

length Λ inside the crystal is:
$$p(\Lambda) = \frac{e^{-\frac{\Lambda}{\Lambda_e}}}{\int_0^{\infty} e^{-\frac{x}{\Lambda_e}} dx} \quad (23)$$

We calculate the penetration Λ for each ray by Monte Carlo sampling the probability distribution given by Eq.(23). The reflected ray direction is calculated by using the specular reflection laws considering the

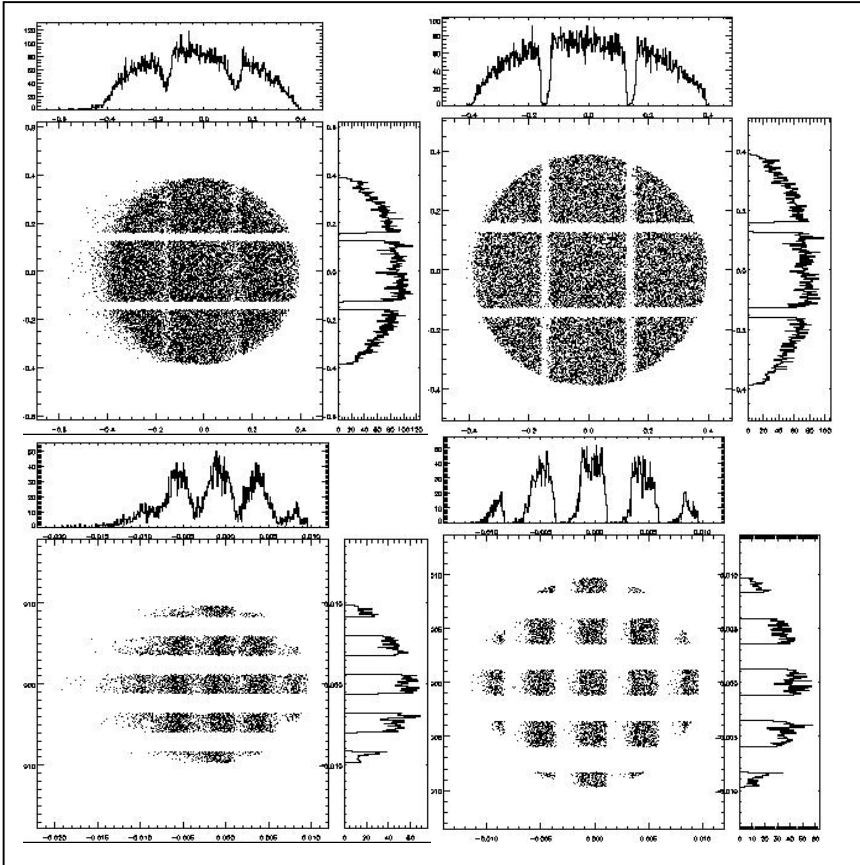


Fig 6. Effect of the penetration length in the crystal. Top: Image of a grid of 120 μm periodicity and 14 μm wire thickness using the basic configuration. The penetration length is 500 μm (left) and 100 μm (right). Bottom: Image of a grid of 2 μm periodicity and 1 μm wire thickness using the basic configuration. The penetration length is 25 μm (left) and 5 μm (right). We observe that resolutions of about 10 μm can be obtained with penetration depths of few hundreds μm and submicron resolution is possible with penetration depth of few μm .

normal to the crystal at the intercept point. We have performed several runs for the basic configuration with different values of Λ_e . Results show that Λ_e less than 100 μm do not alter significantly the quality of the image (see Fig. 6a). This result suggested the question if it could be possible to obtain sub-micron resolution using a XCIM. To demonstrate this hypothesis, using the basic configuration with a point source, we have imaged a grid with 2 μm period and one μm wire thickness. The magnified image of such a grid (Fig 6b), is computed using Λ values of 5 and 25 μm (the order of the primary extinction length for perfect crystals like Si or Ge). From these images it is evident that the one-micron features of the grid are perfectly resolved. Note that the penetration depth creates an asymmetry in the wire profile: it deforms more one edge than the opposite one.

4. Experimental results.

In previous papers¹⁸⁻²⁰ we demonstrated that using XCIM it is possible to reach high spatial resolution about 4 μm in the big field of view (some mm^2). Unfortunately in previous experiments magnification was not so big and reached about 4-8 \times . To prove that with XCIM it is possible to receive high magnification special test measurements in present work were done. Laser produced plasmas, generated by the interaction of low power ns excimer laser pulses with a

solid target, were used as X-ray backlighter sources for our test experiments. XeCl excimer laser Hercules^{21,22} was used as laser source. The laser has an energy about 1 J per pulse, a repetition rate of up to 0.5 Hz, a pulse duration of 10 ns and the power density on the target was about 10^{12} W/cm².

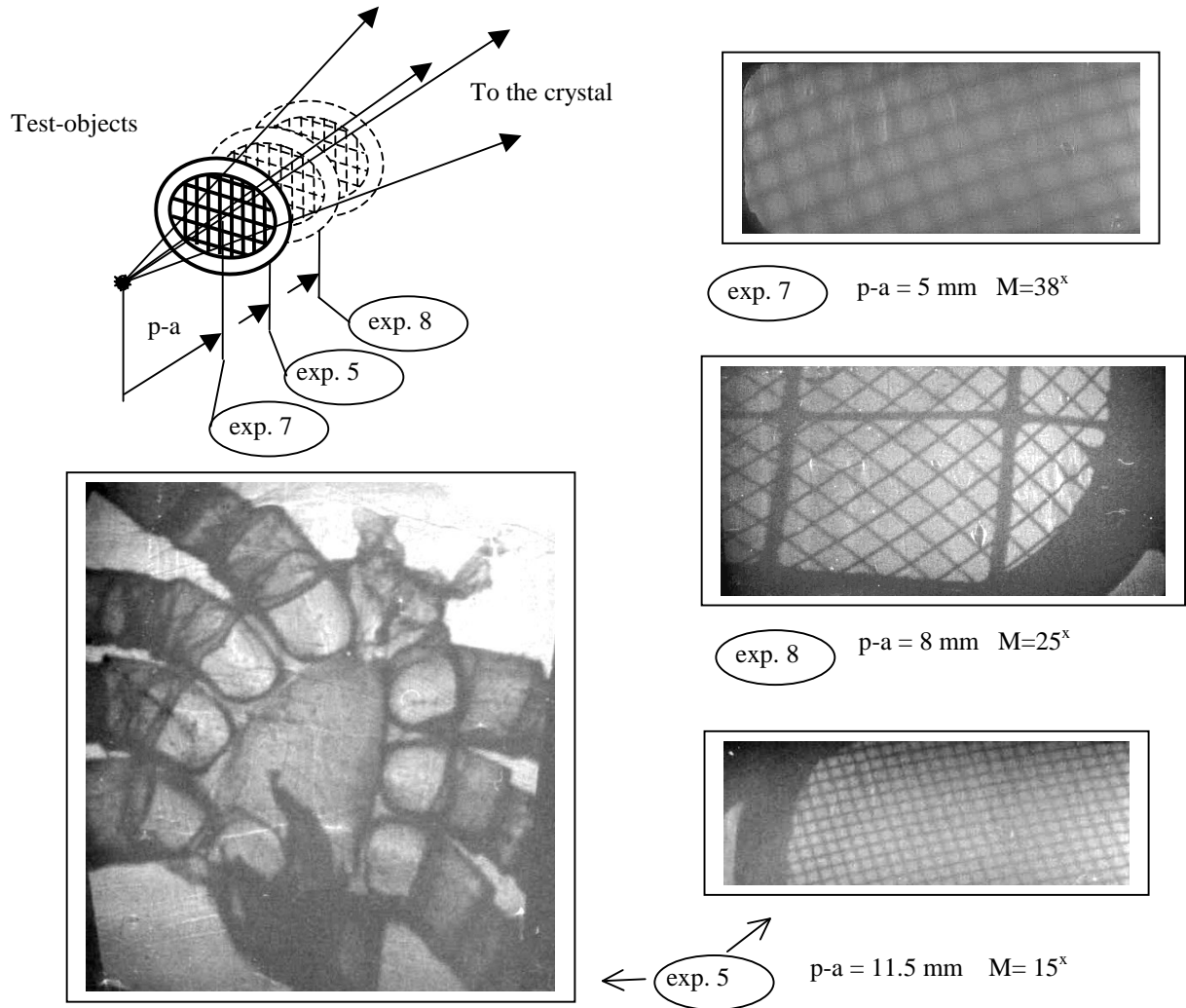


Fig.7 Monochromatic images of different grids (Exp. 8 - thin grid: wire thickness 14 μ m, period 120 μ m; thick grid: wire thickness 60 μ m, period 760 μ m. Exp.5 and 7- wire thickness 10 μ m and 50 μ m) and a spider, obtained by the XCIM scheme at the wavelength ~ 11.5 \AA ($\theta = 35.7^\circ$) with different magnifications. A XeCl laser with pulse energy of 1.0 J and duration of 10 ns heated solid Cu target.

In our experiments we have used mica spherically bent crystals ($2d \approx 19.9$ \AA) with radii of curvature of $R=150$ mm and aperture size of 15 mm x 50 mm²²⁻²⁵. The crystals were used in the first order of reflection. All distances for the experimental setup were obtained in according with equations (3) ÷ (6). By choosing the proper target material and laser intensity, we have been able to create intense soft X-ray radiation in the desired X-ray spectral range. The most efficient lines for monochromatic backlighting, are the intense resonance lines of ions of different elements. In our case we have used the emission of resonance lines of Ne-like of Cu XX, obtained under interaction of solid targets with XeCl laser radiation. Different grids were used as test-objects. In all experiments, the images were detected on Kodak RAR-2492 X-ray film. It was necessary to expose the film to around 300 shots of XeCl laser to collect appropriate intensity for high contrast images.

The main idea of present experiments was to demonstrate that with fixed following parameters: Bragg angle θ , distance source crystal p , and distance crystal film b - it is possible to receive images with different magnification just due to the changes of distance between source and test object (mesh(es) or biological) $p-a$. In this case during all presented experiments

we keep Bragg angle $\theta = 35.7$ degree, $p= 93$ mm, $b=260$ mm (unfortunately it was the biggest distance which we could put inside the vacuum chamber). In exp. 7 the distance p-a was about 5 mm and we had magnification about 38^{\times} . The mesh has $10 \mu\text{m}$ wires with period $50 \mu\text{m}$. In exp. 5 we had distance p-a about 8 mm and we had magnification about 25^{\times} . The smallest mesh, which will be good to model has wires $14 \mu\text{m}$ and period $120 \mu\text{m}$. In exp. 8 the distance p-a was about 11.5 mm and we had magnification about 15^{\times} . The test mesh the same like in experiment 5 has $10 \mu\text{m}$ wires with period $50 \mu\text{m}$. Experimentally obtained images are presented on Fig. 7.

Table. 5. Results of image magnification and spatial resolution modeling..

Exp #	p-a [mm]	Mesh period [μm]	Mesh thickness [μm]	M (exp)	M	$M_{\text{src tan}}$	$M_{\text{src sag}}$
7	5	60	10	38	33.4	31.14	37.02
5	8	120	14	25	20.9	17.6	23.5
8	11.5	50	10	15	14.5	10.8	16.7
Source size (μm)		Spatial resolution in (μm)					
		Exper. 7		Exper. 5		Exper. 8	
		fd	ft	fd	ft	fd	ft
100		65	80	59	81	52	84
50		32	37	26	39	25	42
25		16	20	13	20	13	22
10		7	10	6	7	8	10
0		1.3	1.6	1.5	1.4	2.5	3

For comparison with obtained experimental results ray tracing modeling were carried out. It was selected the following optical setup close to experimental one: distance source-crystal is $p=9.3$ cm. Bragg angle is $q=35.7$ deg. Crystal radius is $R=15.94$ cm, distance crystal to image plane is $b'=26$ cm. Results of image magnification and values of spatial resolution for three different experiments are presented in Tab. 5. We could see good coincidence between experimental and modeling values for obtained image magnifications.

Results of modeling also presented on Fig.8,9. It was used an isotropic source with a divergence of 0.1 rad. It illuminates a surface of the crystal about $1.4 \times 0.8 \text{ cm}^2$ centered in the crystal center. We have used source sizes of dimensions (**diameter**): **0 (point), 25, 50 and 100 μm** .

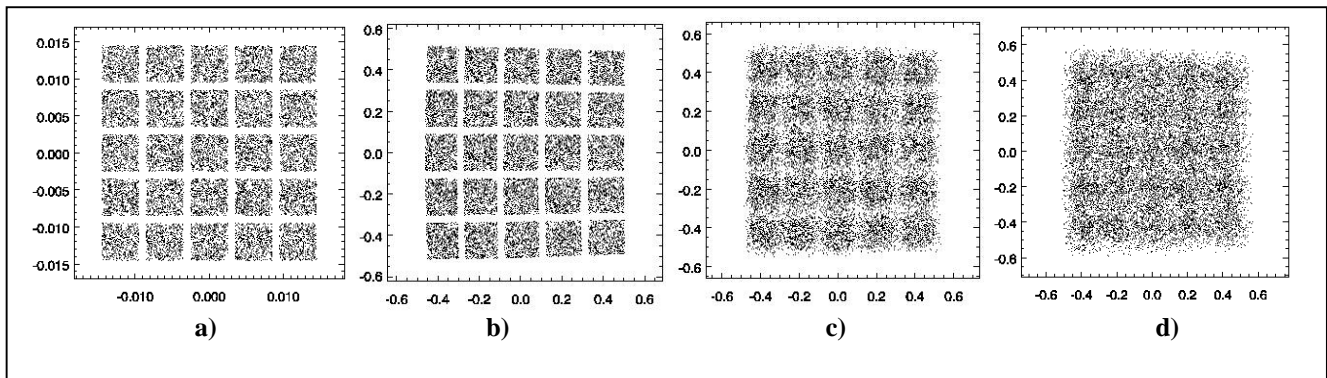


Fig.8 Ray-tracing modeling for the parameters of Exp. 7. a) Ray tracing image at the mesh position. Images obtained using the following size of sources: b) 0 (point), c) 25 μm , d) 50 μm .

From comparison experimental and ray tracing modeling results presented on Fig. 7-9 it is clear seen that experimentally obtained with high magnification images has a very sharp edges with spatial resolution better than $10 \mu\text{m}$. It is necessary to mentioned that a big field of view, in which images are good resolved, was obtained. Obtained field of view was bigger than 1 mm^2 and was limited not by XCIM scheme property, but limited by the size of used crystal. It is also clear seen that experimentally obtained images had slightly different spatial resolution for different directions. Such result is in a very good coincidence with ray tracing modeling prediction.

It is necessary one more underline very important feature of the XCIM scheme, which is the possibility to image not only a plane objects, but also a 3D objects; like a plasma, biological or other structured objects with finite thickness. Such unique property of XCIM scheme is clear seen from image of biological object –spider, presented on Fig.7. Very small details with the sizes smaller than $10 \mu\text{m}$ could be clear seen despite of big thickness of such object. Also we would like to point out, that for all of these experiments, the X-Ray backlighter sources were placed very closed or exactly on the Rowland

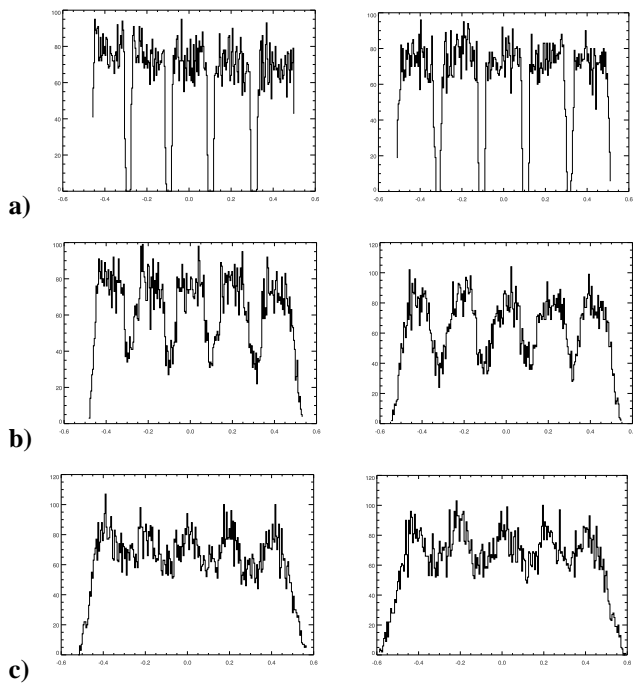


Fig.9 Histograms at the image plane: a) for a source of 0 μm , b) , c) 25 μm , d) 50 μm . Left side: tangential plane. Right side: Sagittal plane

circle. Very important that in all our experiments the object-crystal distances were smaller than f , i.e. in the region, where for usual optics it is impossible to have imaging. Nevertheless, using the SMB scheme, high quality images were obtained.

IV. Conclusion

It was demonstrated both experimentally and by ray-tracing modelling, that the considered X-ray Crystal Imaging Microscope (XCIM) allows us to extend the monochromatic backlighting spectral range, due to the possibility to operate in a wide range of Bragg angles ($20^\circ < \Theta < 90^\circ$ and even smaller angles). Using the currently available spherically bent crystals, it is practically possible to perform X-Ray backlighting experiments with any wavelengths in the 1-18 \AA spectral range. The XCIM requires X-ray sources similar to the traditionally used backlighter X-ray source.

The main advantage of the proposed microscope is in the simultaneous achievement of:

- 1) High spatial resolution of up to 1-2 μm .
- 2) The high resolution is obtained over a large field of view of about 1-2 mm^2 . Even larger fields of view can be achieved using the same technique.
- 3) Images of thick objects can be obtained with high spatial resolution over all object parts. Very simple alignment, compared to the traditionally used X-Ray monochromatic backlighter

scheme based on spherically bent crystals. Also, the experimental layout is much smaller (for the same magnification), thus a smaller experimental vacuum chamber is needed. 4) It is possible to use practically any bright line in the spectral range 1-18 \AA as a monochromatic backlighter X-Ray source.

The XCIM can be used for the investigation of relatively large objects, like different plasmas (z-pinch, liner plasmas, laser produced plasmas, ion beam generated plasmas and plasmas in shock-wave related experiments), biological objects, and other structured objects. It may become a useful experimental tool in the near future, when experimentally realized plasma sizes will reach 10 mm^3 or more, and the plasma homogeneity will have to be determined with superb spatial resolution.

References

1. "X-ray microscopy and spectromicroscopy", J. Thieme, G. Schmahl, D. Rudolph and E. Umbach (editors) Springer, Berlin (1998).
2. K. Yada and S. Takahashi, in "X-ray microscopy II", D. Sayre et al. (editors), 323, Springer Verlag (1988)
3. J. Kirz, C. Jacobsen, and M. Howells, Q. Rev. Biophys. **28** 1 (1995)
4. P. Dhez, P. Chevallier, T.B. Lucatorto and C. Tarrío, Rev. Sci. Instrum. **70** 1907 (1999)
5. V.E. Cosslet, A. Engstrom and H.H. Pattee "X-ray microscopy and microradiography" Academic, New York, (1957)
6. V.E. Coslett and W.C. Nixon, "X-ray microscopy" Cambridge Univ. Press, Cambridge (1960).
7. G. Schmahl, D. Rudolph, P. Guttman, G. Scheider, J. Thjeime and B. Niemann, Rev. Sci. Instrum. **66**, 1282 (1995)
8. S.A. Pikuz, T.A. Shelkovenko, V.M. Romanova et al. Rev. Sci. Instrum. **68**, 740 (1997)
9. Y. Aglitskiy, T. Lehecka, S. Obenschain, C. Pawley, C.M. Brown and J. Seely, Rev. Sci. Instrum. **70** 530 (1999)
10. M. Sanchez del Rio, A. Ya. Faenov, V. M. Dyakin et al. Physica Scripta **55** 735-(1997)
11. J.A. Koch, O.L. Landen, T.W. barbee et al. Applied Optics **37**, 1784 (1998)
12. Y. Aglitskiy et al. Appl. Opt. **37**, 5253 (1998)
13. J. Workman, S. Evans, G.A. Kyrala. Rev. Sci. Instrum. **72**, 674 (2001)
14. E. Förster, K. Gäbel and I. Uchmann, in "X-ray microscopy III" A. Michette et al. (editors), 202-205, Springer (1992)
15. P. Kirkpatrick and A. V. Baez, J. Opt. Soc. Am., **38** 766 (1948)
16. M. Sanchez del Rio, M. Fraenkel, A. Ziegler, A. Ya. Faenov and T.A. Pikuz, Rev. Sci. Instrum. **70**, 1614 (1999)
17. C. Welnak, G.-J. Chen and F. Cerrina, Nucl. Instrum. Meth. **347**, 338 (1994)
18. M. Fraenkel, A. Ziegler, A. Ya. Faenov, T. A. Pikuz, Physica Scripta **59** 246 (1999);
19. T.A. Pikuz, A. Ya. Faenov, M. Fraenkel et al. SPIE Proceedings **3767**, 67 (1999) ;
20. T.A. Pikuz, A. Ya. Faenov, M. Fraenkel et al. Laser and Particle Beams (accepted).
21. S. Bollanti, R. Cotton, P. Di Lazzaro et al., *Il Nuovo Cimento* **18D**, 1241 (1996)...
22. S. Bollanti, P. Albertano, M. Belli et al. *Il Nuovo Cimento* **20D**, 1685(1998).